Velocity distributions of particles sputtered from supported two-dimensional MoS_2 during highly charged ion irradiation

Lucia Skopinski,[1,*] Silvan Kretschmer,[2] Philipp Ernst,[1] Matthias Herder,[1] Lukas Madauß,[1] Lars Breuer,[1] Arkady V. Krasheninnikov,[2,3] and Marika Schleberger[1,†]

[1]*Fakultät für Physik and CENIDE, Universität Duisburg-Essen, 47057 Duisburg, Germany*

[2]*Institute of Ion Beam Physics and Materials Research, Helmholtz-Zentrum Dresden-Rossendorf, 01328 Dresden, Germany*

[3]*Department of Applied Physics, Aalto University, 00076 Aalto, Finland*

(Received 13 October 2022; accepted 30 January 2023; published 14 February 2023)

A key problem in ion-solid interaction is the lack of experimental access to the dynamics of the processes. While it is clear that the mechanisms of interaction and sputtering depend on the kinetic and potential energy (sum of ionization energies) of the projectile, the importance and interplay of the various interaction mechanisms are unknown. Here, we have irradiated substrate-supported (Au, SiO_2) monolayers of MoS_2 with highly charged xenon ions (HCIs; charge state: 17+ to 40+), extracted the emitted neutral postionized Mo particles in a time-of-flight mass spectrometer, and determined their velocity distributions. We find two main contributions, one at high velocities and a second at lower velocities, and assign them to kinetic and potential effects, respectively. We show that for slow HCIs (5 keV) the interaction mechanisms leading to particle emission by electronic excitation and momentum transfer, respectively, are independent of each other, which is consistent with our atomistic simulations. Our data suggest that the predominant mechanism for potential sputtering is related to electron-phonon coupling, while nonthermal processes do not play a significant role. We anticipate that our work will be a starting point for further experiments and simulations to better understand the interplay of processes arising from E_{pot} and E_{kin}.

DOI: 10.1103/PhysRevB.107.075418

I. INTRODUCTION

Two-dimensional (2D) materials are expected to be the key elements of many novel devices due to their unique mechanical, electronic, and chemical properties. After the first preparation of graphene in 2004 [1], the number of realized 2D structures has increased to several hundred so far [2]. Apart from improving the synthesis [3,4], a main focus in research lays on the processing and modification of the materials towards the realization of devices. One way to influence their properties is by stacking several monolayers and therefore creating van der Waals heterostructures with tunable or synergistic properties [5,6]. In addition, surface structuring methods, such as beams of various energetic particles, have been suggested and successfully applied for defect engineering [7–10].

While ion beams are an established method to structure thin films or 2D materials, with the latter several problems occur. First, the description by classical models is not straightforward. Sputtering and implantation, e.g., are different due to the absence of a three-dimensional (3D) crystal lattice. Further, atoms sputtered from the substrate can cause severe damage to the 2D monolayer on top [11]. This problem can be circumvented, e.g., by using slow highly charged ions (HCIs) with low kinetic energy (in the keV range) and high potential energy (the sum of the ionization energies). These projectiles deposit their energy into the electronic system of the target material near its surface. It has been shown that HCIs in particular can be applied as an efficient tool for pore creation and material modification. For example, pore creation in freestanding MoS_2 allows for adjustment of the pore radius by tuning the charge state of the primary HCI [12] and pore creation in insulating fluorinated graphene works equally well [13]. Highly conductive, pristine graphene, on the other hand, has been proven to be very resistant as its high electron mobility prevents pore formation due to electronic excitation [14] and may even work as a protective cover [15].

These examples show that the energy dissipation within the 2D material depends strongly on its electronic and thermal properties. However, while different effects for different ion energies have been recognized before [16], the exact physical mechanisms are still a subject of discussion. Especially for semiconducting and insulating targets with lower electron mobility, the high local perturbation in the electronic system caused by neutralization and deexcitation of the impinging HCI is not well understood. In fact, the proposed models range from Coulomb explosion over thermal spike and defect mediated desorption to nonthermal melting (for a review, see [16]). Although these models differ greatly in terms of their spatial and temporal dynamics, the final state is often similar (some fraction of the 2D target material is missing, for example). This means that with the common postmortem analysis techniques one simply cannot distinguish between the models. This lack of direct experimental access to the mechanisms is a key problem, especially when a specific change in a 2D material, whether freestanding, substrate-supported, or heterostructure, is to be achieved via defect engineering.

*lucia.skopinski@uni-due.de

†marika.schleberger@uni-due.de

To shed light on the ion-solid interaction mechanisms, we therefore take another approach. By means of mass spectrometry we study particle emission from a supported 2D material *during* HCI irradiation under UHV conditions. By preparing an ultrathin layer of a semiconductor (i.e., a material sensitive to potential sputtering) on top of a gold substrate (not sensitive to potential sputtering) while maintaining a sufficiently large sample size, we effectively decouple the two effects as well as possible. By varying both the charge state and the kinetic energy of the ion as well as the substrate, we can systematically exploit the parameter space to identify and evaluate the individual contributions. In addition, we study the velocity distribution of particles emitted by HCI irradiation and compare molecular dynamics (MD) simulations that have been performed to further our understanding of the experimental findings. In this way we can rule out Coulomb explosion and nonthermal melting to be the dominant processes for HCIs interacting with semiconducting 2D materials.

II. MATERIALS AND METHODS

A. Sample preparation

As the target material we use monolayer MoS_2 which is the prototypical semiconducting 2D material. The MoS_2 flakes were grown directly on a 300-nm SiO_2/Si substrate by chemical vapor deposition (CVD). To this end, a 1% sodium cholate solution as growth promoter is spin-coated at 4000 rpm for 60 s onto the cleaned (acetone, sonication) SiO_2 substrate. A droplet of a saturated solution of ammonium heptamolybdate in deionized water is deposited onto the substrate and then heated for 24 min at 300 °C to form MoO_3, providing the molybdenum feedstock. The substrate is placed in the center of a 1-in. CVD tube furnace and 40 mg of solid sulfur (Sigma Aldrich; 99.89%) is placed 15 cm upstream of the substrate in a different heating zone. Growth occurs at atmospheric pressure in a flow of 500 sccm of Ar gas (99.999% purity). The furnace temperature is ramped to 750 °C at a rate of 75 °C/min. While the Mo source and SiO_2 growth substrate reach 750 °C, the maximum temperature of the sulfur is 150 °C. After a 19-min growth period, the furnace is opened, and the sample is rapidly cooled to room temperature in 500 sccm flowing Ar. A detailed description of the process and characterization of typical samples can be found in Refs. [17,18].

B. MoS_2 transfer

The transfer of MoS_2 to the Au substrate was accomplished by spin-coating polymethylmethacrylate (PMMA) onto the as-grown sample, which was then placed in a bath of 0.1 M KOH to slowly etch the SiO_2 surface and release the PMMA/MoS_2 layer from the substrate. The floating PMMA/MoS_2 layer was then transferred into successive water baths for cleaning and finally scooped onto the target substrate. The sample was then dried, and the PMMA was removed with an acetone bath.

C. Irradiation and ToF-SNMS

Highly charged xenon ions were generated in an electron beam ion source (EBIS) commercially available from Dreebit GmbH, Germany. To select and modify the beam parameters (see supporting information for detailed beam characterization) a bending sector magnet and a deceleration section described in Ref. [19] have been used. Due to ion irradiation sputtered sample particles are postionized by an Excimer laser (ExciStar XS by Coherent) with a wavelength of 157 nm. The laser beam is shot parallel to the sample surface with a distance of 1.2 mm and has a beam diameter of 0.21 mm. The ionized particles are extracted into a time-of-flight (ToF) mass spectrometer. This method is called secondary neutrals mass spectrometry (SNMS). We vary the extraction delay between the time of HCI impact and extraction into the spectrometer and probe which particles have reached the laser volume in each case. From every mass spectra the ^{98}Mo peak was evaluated and is fitted in Figs. 1 and 3 normalized to the number of primary HCIs per pulse (see Appendix B for primary pulse characterization) as a function of the extraction delay. For the measurements with Xe^{17+} and Xe^{37+} at a kinetic energy of 5 keV as well as Xe^{28+} at 260 keV the determined number of ions per pulse had to be corrected after the measurement series. The correction factor is indicated in the corresponding figure. The data shown in Figs. 1, 3, and 4 has been smoothed by Lowess filters with OriginLab 2019b to reduce noise. The description and Fig. 6 in Appendix A give an impression of the non-smoothed data.

D. MD simulations

Empirical potential MD simulations using the LAMMPS package [20] are carried out to model 5 keV Xe ion impact on 2D MoS_2 supported by gold substrate. For MoS_2 either reactive bond order (REBO) potential [21] or the Stillinger-Weber (SW) potential [22] are used to parametrize the interactions of Mo and S atoms; the results turn out to be qualitatively comparable. The Au(111) substrate is modeled using the embedded atom method potential [23]. van der Waals (vdW) interactions of the 2D material and the substrate are taken into account by Lennard-Jones (LJ) potentials with the parameters fitted to the PBE-vdW calculations given in Table I below.

The interaction with the high energetic ion and interactions at close separations are parametrized by the Ziegler-Biersack-Littmark (ZBL) potential [24] (smooth joining for REBO, SW). The considered model system consists of the 2D material on a 3.5-nm-thick Au(111) substrate. The lateral extension of the simulation box amounts to 18.3×15.8 nm^2, which results in simulations comprising 75 k atoms in the simulation box. As in previous studies the impact energy is dissipated by Berendsen thermostats at the boundaries of the simulation box. During the MD run all atoms passing the top boundary region are accounted for together with their velocities. The statistics of the Mo velocity distribution is collected from 1200 ion impacts distributed over 240 impact points which are selected in the irreducible area.

III. RESULTS AND DISCUSSION

For our study we have chosen monolayers of MoS_2, as this is the best investigated 2D material apart from graphene. In contrast to graphene, its constituent Mo can be unambiguously detected by our mass spectrometer and the material is thus well suited for our purposes. The experimental setup has

TABLE I. Parameters of the Lennard-Jones (LJ) interatomic potential. For $r < r_c$ the LJ potential $V(r) = 4\varepsilon[(\frac{\sigma}{r})^{12} - (\frac{\sigma}{r})^{6}]$ models the attractive dipole-dipole interaction which keeps the 2D material in place on top of the substrate. The repulsive part of the LJ at close separation is dominated by the Ziegler-Biersack-Littmark potential. The potential parameters were obtained by first-principles simulations, where ε denotes the interaction strength, σ is the zero-crossing distance of the potential with the minimum being at $r_{\min} = 2^{1/6}\sigma$, and r_c defines the cut-off radius.

	ε (meV)	σ (Å)	r_c (Å)
S-Au	4.48	3.264	9.3025
Mo-Au	2.03	2.282	8.1850

been described in detail elsewhere [19], and here we will only briefly summarize its main capabilities. Our ultrahigh vacuum setup is based on a reflectron type time-of-flight mass spectrometer, designed to analyze secondary particles emitted during ion irradiation. We use an electron beam ion source to produce bunches of ions with various charge states q (here between Xe^{17+} and Xe^{40+}) and a deceleration/acceleration section to tune the kinetic energy of the ions (here 5 keV and 260 keV). In addition, our setup is equipped with a pulsed excimer laser for postionization of the sputtered particles, since most of them are emitted as neutral particles. By delaying postionization and extraction with respect to the time of impact of the ion pulse on the sample – corresponding to a measurement of time-of-flight mass spectra at different extraction delays – we can obtain mass and velocity distributions of the emitted neutral particles. For the data that we will present in the following, from each spectrum the intensity of the ^{98}Mo mass peak was evaluated and plotted as a function of the extraction delay. The higher the extraction delay of a signal, the lower the velocity at which the associated particle moves away from the sample surface. Note that we obtain the velocity distribution from the flight time distribution and that for a quantitative analysis a very time-consuming optimization of the setup would be required. For the purpose of this paper it is, however, sufficient to analyze the relative numbers and we therefore refrain from plotting absolute velocities except for the comparison with our simulations.

A. Dependence on the potential energy

We begin by presenting and discussing the data obtained in the experiments on irradiation of MoS_2 on Au (see the Materials and Methods section for preparation) with Xe^{q+} ions at a low kinetic energy of 5 keV. In this case we expect some energy transfer to the sample via nuclear collisions $E_{\text{kin}}^{\text{nuclear}}(q)$ while there should be almost no electronic contribution $E_{\text{kin}}^{\text{electronic}}(q)$ due to the low velocity of the ion. By varying the charge state and therefore the potential energy of the ion we change the deposited energy $E_{\text{dep}}^{\text{pot}}(q)$ which is known to be deposited within the first few layers of the sample material [25,26].

Figure 1 shows the intensity of emitted neutral Mo particles during the irradiation per primary HCI as a function of the extraction delay of the corresponding mass spectra. The purple curve stands for the irradiation by 5 keV Xe^{17+} ions,

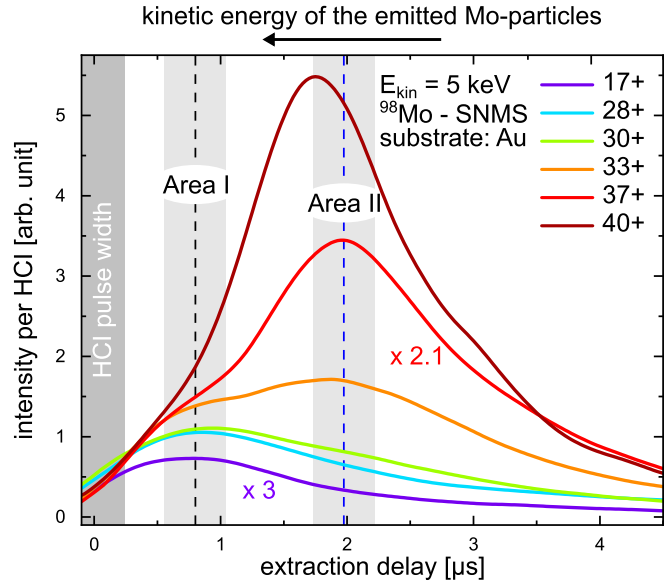

FIG. 1. Intensity of the ^{98}Mo signal as a function of the extraction delay for different charge states. Correction factors of 3 (Xe^{17+}) and 2.1 (Xe^{37+}) have been used to account for HCI-current calibration difficulties (see Appendix A). The marked gray areas depict contributions of kinetic (area I) and potential (area II) energy to the emission process. The dark-gray area shows the estimated pulse width of the HCI pulse.

being equivalent to a potential energy of $E_{\text{pot}} = 3.0$ keV, as the lowest charge state used. The measured data of the Mo signal shows one maximum at the extraction delay $t_{\text{extraction}} = (842.9 \pm 10.5)$ ns. As the potential energy is significantly smaller than the kinetic energy, we assume that the latter has the greatest influence on the emission process. We therefore assign the higher velocity Mo particles in the region marked "area I" to the kinetic sputtering process originating from a linear collision cascade [27]. This obviously changes when the contribution of the potential energy increases. The measured signals change significantly with respect to the shape, intensity, and position of the maximum for the charge states q between 28 and 40. Around the extraction delay of 1.975 µs, a second contribution to the signal develops, which strongly increases with a increasing charge state of the HCI. For the Xe^{40+} irradiation with a potential energy of $E_{\text{pot}} = 38.5$ keV, which is almost seven times greater than the kinetic energy ($E_{\text{kin}} = 5$ keV), this additional contribution dominates the spectrum with its maximum at $t_{\text{extraction}} = (1684.1 \pm 3.2)$ ns, marked as "area II."

Overall, we observe that an increase in the potential energy of the HCI, and therefore the electronic excitation energy $E_{\text{dep}}^{\text{pot}}(q)$ of the sample, clearly enhances the total yield of emitted Mo particles. This effect has been found for 3D materials such as LiF and has been coined *potential sputtering* [26]. That we can identify a similar process here in a 2D material, underlines the fact that the energy deposition is indeed limited to the very first few layers. In addition, we find that the increase in number of sputtered particles is due to a significant contribution of particles with a lower emission velocity (area II) than those assigned to a kinetic sputter mechanism (area I).

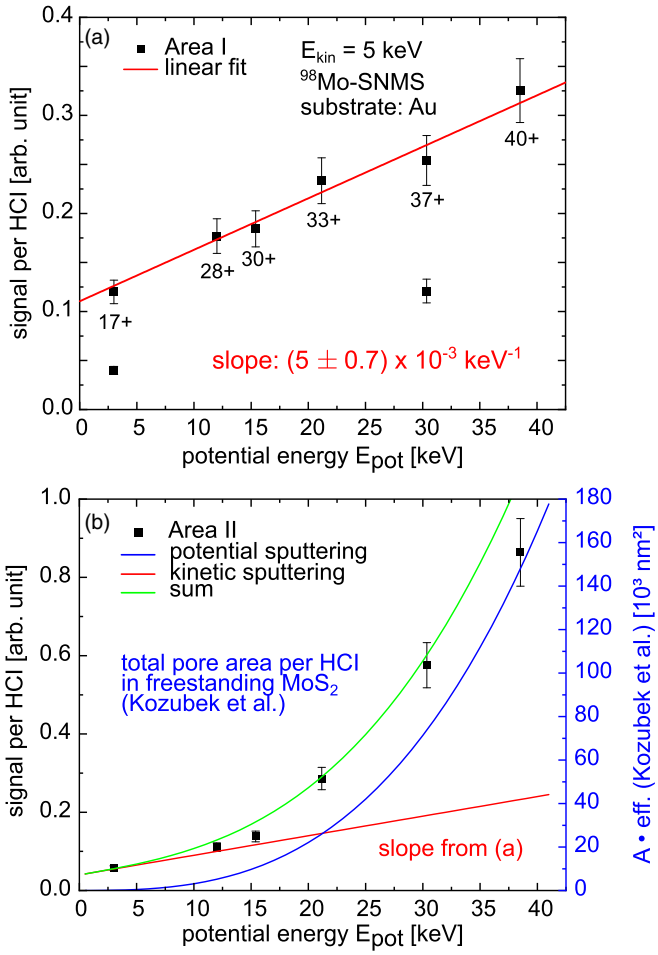

FIG. 2. Evaluation of area I (a) and area II (b) in Fig. 1 as a function of the potential energy of the projectile. The data in (a) can be described by a linear fit of slope $m = 5\times10^{-3}$ keV^{-1}. Comparison of the signal due to potential sputtering [area II, (b)] with the results for potential sputtering of MoS_2 by Kozubek *et al.* [12]. The green curve is the sum of potential sputtering (blue) and kinetic sputtering [red; a linear dependence with the same slope as in (a) was used here].

We will discuss this important finding in more detail in the following paragraph. Since the transmission through our spectrometer is energy dependent, we selected two areas with sputtered particles of a different energy and only relate intensities from the same area. In Fig. 2 we plot the signal at the fixed emission energies (areas I and II) as a function of the potential energy of the HCI (corresponding to its charge state).

From Fig. 2 it is obvious that particle emission in the two areas exhibits a different dependence on the amount of deposited potential energy. In area I (0.8 μs), we observe a linear dependence of the signal on the potential energy of the projectile. The fit shown in Fig. 2(a) has a slope of $(5\pm0.7)\times10^{-3}$ keV^{-1}. In contrast, the signal in area II (1.975 μs) increases more strongly with the potential energy of the primary HCI. Many previous studies on the interaction of HCIs with surfaces identified the so-called threshold values for the creation of defects (for a detailed overview, see Aumayr *et al.* [16]). Our data indicates that potential sputtering can be detected even for the smallest charge states we have used and becomes the dominant mechanism for the emission of slow particles by projectiles with a potential energy of more than E_{dep}^{pot} $(q = 30) = 17$ keV.

After having observed the transition from and to kinetic and potential sputtering mechanisms in the emission process, the question arises, whether we can unravel their interplay and interdependency, respectively. If, e.g., there was sufficient potential energy deposited into the 2D material and the resulting sputtering process would be fast enough, all of the sample material will have been emitted, before the emission on the basis of the linear cascade sets in. That is, a linear cascade can still take place in the substrate, but there would no longer be any sample material left to be affected. We observe from our data, that even for the highest charge state, Xe^{40+}, the signal in area I (identified as originating from kinetic sputtering) remains more or less unchanged. The small increase in area I with increasing potential energy is most likely due to a widening of the signal from area II upon increase. We thus deduce that the deposition of potential energy has no significant effect on the processes related to kinetic sputtering. There are several possible reasons for this, e.g., (i) the excitation of the target material by the HCI is in general too weak, (ii) the excitation has already decayed, or (iii) is still building up. While electronic excitation is clearly strong enough to sputter particles, we will consider the different timescales of proposed models to describe the interaction of HCIs with solids in the following section.

Next, we will discuss the superlinear behavior observed in area II. In Fig. 2(b) we used a combination of the linear fit determined by fitting the data in Fig. 2(a) and the dependence of pore radius in MoS_2 as a function of potential energy as determined by Kozubek *et al.* [12]. In this work we used high-resolution scanning transmission electron microscopy to analyze the pore formation in freestanding MoS_2 irradiated by HCI and revealed a linear dependence of both, the pore radius and the efficiency of pore formation, on the potential energy of the HCI [12]. The total pore area as a product of the pore area and efficiency is shown in Fig. 2(b) in blue. Since kinetic sputtering processes driven by elastic collisions of the nuclei are strongly reduced in freestanding samples because of their true 2D nature, we assume that the determined dependence represents exclusively the potential effects. For our sample of substrate-supported MoS_2, we clearly have to account for the substrate-driven kinetic sputtering. The linear fit in Fig. 2(a) that has been transferred to Fig. 2(b), is an attempt to account for exactly this contribution. The sum of kinetic sputtering due to the substrate and potential sputtering measured for a freestanding sample matches the data very well. We find no indications for synergistic effects. We therefore conclude that for the sputtering of supported 2D MoS_2 by slow HCIs, effects from potential sputtering simply add up to those from kinetic sputtering.

Several possible mechanisms for potential sputtering have been suggested. Many of them have originally been applied to describe the electronic excitation of solids via swift heavy ions. In this case, the projectiles are so fast, that the scattering cross section for nuclear collisions is practically zero and the slowing down of particles (stopping) happens via electronic excitations and ionization of target atoms. This is very different from HCIs, but the dominant electronic

excitation and similar irradiation-induced morphologies [16] have led researchers to use the models anyhow.

One possible scenario, the so-called "Coulomb explosion" is a burst of material due to Coulomb repulsion of the positively charged atoms around the point of impact where electrons have been depleted by the HCIs. Multiply charged secondary ions or clusters could thus be an indication of such a Coulomb explosion [28]. Further, mechanistic arguments as well as model calculations predict the emission of rather energetic particles [29], which is in clear contrast to our observations.

Defect-mediated desorption is observed in materials where a self-trapped exciton forms upon irradiation like in alkali halides or in SiO_2. In our case, this mechanism seems highly unlikely, as the Au substrate would efficiently quench any excitonic processes (typically no photoluminescence spectroscopy signal is observed from these samples) [18].

Another possibility is the so-called nonthermal melting, describing the destabilization of atomic bonds caused by the direct promotion of electrons from bonding valence band into antibonding conduction band states [30]. This scenario has been intensively discussed to explain laser ablation [31]. In this case, two mechanisms are relevant, again Coulomb explosion as a consequence of the electron emission due to the strong electronic excitation, and the direct emission of atoms from an electronically repulsive state with extremely low, subthermal energies on a subpicosecond timescale. If the latter was dominant, we would expect that the effective contribution from kinetic sputtering (area I) should decrease with increasing potential energy as atoms would be efficiently ejected before the collisional cascade sets in.

Finally, the thermal spike model assumes the dissipation of the electronic energy via energy transfer to the lattice atoms. This is described in terms of a lattice temperature and the typical structural changes can be associated to phase transitions like, e.g., melting [32–34]. The velocity distributions obtained in our experiments indicate a large fraction of particles emitted at energies comparable to thermal emission, which increases with increasing charge state.

B. Dependence on the kinetic energy

In the following section we will present and discuss the case where the kinetic energy plays a more dominant role. To this end, we repeated the experiment with faster 260 keV HCIs with the same charge states. As presented in Fig. 3, we observe a shift of the highest intensity towards later extraction delays for the lowest charge state; but again, a strong increase in the intensity with increasing potential energy of the HCIs. We start our analysis again with the lowest charge state (Xe^{26+}, $E_{pot} = 9$ keV) as the influence of the kinetic energy ($E_{kin} = 260$ keV) can be best observed there. The position of the maximum (black dashed line in Fig. 3) is with 1.35 µs, about 0.55 µs later than for the 5-keV measurement. With a similar charge state, the maximum is shifted towards particles emitted at lower velocities. This means that the velocity distribution already changes independently of the charge state – only because of the higher velocity of the impinging ion. Due to the increased kinetic energy of the projectile, area I can no longer be assigned to the linear cascade regime, but must be attributed to a collisional spike.

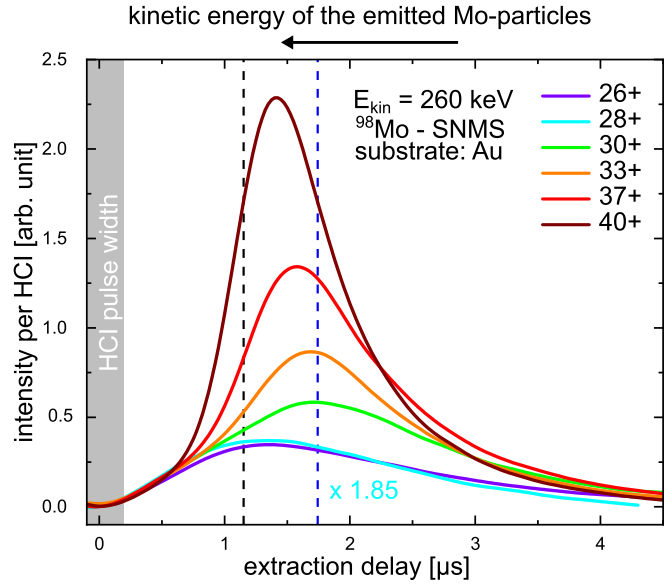

FIG. 3. Intensity of ^{98}Mo particles emitted from a monolayer MoS_2/Au sample during irradiation with 260 keV HCIs as a function of the extraction delay. A correction factor of 1.85 has been used for the Xe^{28+} measurement to account for current calibration issues (see Appendix A). The half maximum width of the widest primary ion pulse used in this experiment $t(Xe^{33+}) = 397.3$ ns is highlighted in dark gray at the extraction delay $t_{extraction} = 0$ µs. The two areas of particular interest are marked by black and blue lines.

Those kinetic interactions are well studied, e.g., Seah showed that the sputter yield of gold by irradiation with Xe projectiles for velocities over 100 keV can be described by adding a spike contribution [35]. Figure 3 also shows that the increase in potential energy clearly leads to an intensity increase. For Xe^{30+}, it starts at around 1750 ns (blue dashed line) with almost the same extraction delay as area II for the Xe 5-keV measurement series. For even higher charge states, the maximum shifts further towards smaller extraction delays, i.e., that while the potential energy still leads to an additional contribution by slower particles, their velocity seems to increase slightly with the charge state of the projectile. This could be due to a synergy effect as the thermal spike overlaps with the collisional spike in time and in space.

C. Dependence on the substrate

To further understand the dependence on the kinetic energy of the projectile, we compared the Mo particles sputtered from single-layer (SL) MoS_2 transferred onto two different substrates, i.e., gold and silicon dioxide. For each system, the smallest and largest charge state used for $E_{kin} = 5$ keV and $E_{kin} = 260$ keV, are summarized in Fig. 4. For better comparability and to eliminate the sources of error in the primary ion normalization, Fig. 4 shows the smoothed and area-normalized (0–6 µs) SNMS data set for the Au substrate (a) and the SiO_2 substrate (b). Dashed lines represent the smallest and the solid lines the highest charge states. Please

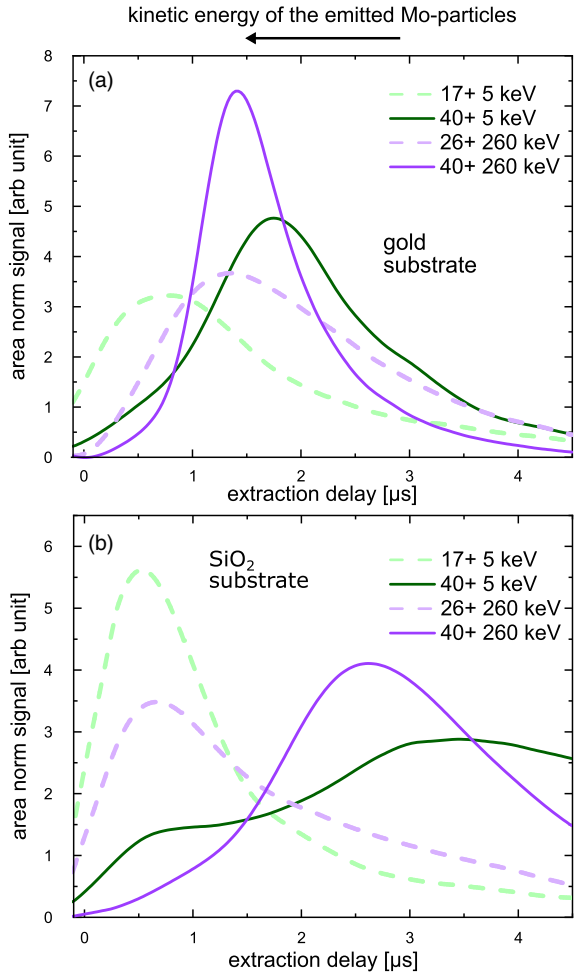

FIG. 4. Area-normalized (0–6 µs) intensity of ^{98}Mo particles emitted from (a) a SL MoS_2/Au sample and (b) a SL MoS_2/SiO_2 sample during bombardment with $Xe^{17+}_{5\,keV}$ (dashed green), $Xe^{40+}_{5\,keV}$ (green), $Xe^{26+}_{260\,keV}$ (dashed purple), and $Xe^{40+}_{260\,keV}$ ions (purple). Plotting against the extraction delay allows slower and faster particles to be distinguished.

note that while we will focus in the following on the shift in the contribution of slower Mo particles, we want to emphasize that an increase in the energy of the projectile, both kinetic and especially potential, always results in an increase of the Mo yield. This agrees perfectly well with our earlier results on the interaction of HCIs with freestanding MoS_2 [12] and with supported hexagonal boron nitride [36].

Figure 4(b) shows that for both kinetic energies the position of the maximum differs significantly for the smallest and the highest charge state. For the charge states $Xe^{17+}_{5\,keV}$ and $Xe^{26+}_{260\,keV}$, the maximum is at an earlier extraction delay (<1 µs) than for $Xe^{40+}_{5\,keV}$ and $Xe^{40+}_{260\,keV}$ (>2 µs).

In the previous discussion, the positions of the maxima in the velocity distributions were either found in area I or area II. Area I was assigned to the kinetic energy dominating the emission process and area II to the potential energy being most relevant. As already discussed, for the Au substrate [Fig. 4(a)], this clear distinction works well for the Xe 5-keV measurement series. The maxima of the Xe 260-keV measurement series, on the other hand, are found almost at the same extraction delay, which we attributed to the occurrence of a collisional spike in the gold substrate at this kinetic energy. In contrast, for a SiO_2 substrate [Fig. 4(b)], the data shows clearly distinct positions of maxima for both charge states at both kinetic energies. From our discussion above, we would thus infer that in SiO_2 there is no indication for a collisional spike. Obviously, the nature of the emission processes therefore does not only depend on the kinetic energy but also on the substrate underneath the 2D sample.

Due to the nature of a 2D material this is not so surprising and in agreement with earlier findings. Theoretical simulations show that the substrate can indeed be the key to the modification of a supported 2D material due to sputtering by backscattered ions, sputtered substrate atoms [11], or by, e.g., a change of strain [37]. To compare the two substrates, we carried out calculations with the program Stopping and Range of Ions in Matter (SRIM) [38] for 260-keV Xe ions in a monolayer of MoS_2 on a substrate. We find a nuclear stopping power of 5.7 keV/nm for a gold substrate and of 2.59 keV/nm for a SiO_2 substrate. The higher efficiency for the transfer of kinetic energy from the ion to the substrate lattice in the case of gold makes it reasonable that we observe the signature of a collisional spike for the gold substrate but not for the SiO_2. Remarkably, however, we observe no indication that the contribution from potential sputtering of the monolayer MoS_2 is affected by the substrate. In principle, the response of the two substrates, one being a metal and the other an insulator, towards irradiation with HCIs should be fundamentally different [26]. Part of the explanation might be that due to the preparation procedure used here, a layer of intercalated water might be present [18,39]. It could act as a protective coating between the 2D material and its substrate. Nevertheless, we believe the main reason to be the extremely shallow energy deposition, which was just recently again demonstrated by Schwestka *et al.*, where pore creation via HCI irradiation was achieved with atomic depth precision [15].

In order to better understand the experimental finding of the kinetic energy driven sputtering mechanism at low charge states we carried out MD simulations of 5-keV Xe ion impacts on MoS_2 supported by Au(111) substrate. Empirical potential MD accounts for the nuclear stopping of a neutral projectile only and can therefore be used to view the limiting case of neutral projectile impinging on the system of interest. A detailed description of the simulation setup can be found in the Materials and Methods section. Figure 5 displays the extracted kinetic energy distribution of the sputtered Mo atoms in comparison with the experimental data from Fig. 1 transformed into a velocity distribution. The simulations were carried out with two different interaction potentials for the MoS_2 sheet, such that strong dependence on the empirical potential can be ruled out. The simulation results show a much broader distribution at higher recoil energies compared to the experimental data for higher charge states. This supports the picture of ejecting fast Mo atoms from ballistic collisions for low charge state and high kinetic energy. With increasing charge state the maximum value of the recoil distribution grows and shifts to lower values – the higher the charge state the more low energy Mo recoils are measured – and disintegration of the MoS_2 sheet is dominated by potential sputtering.

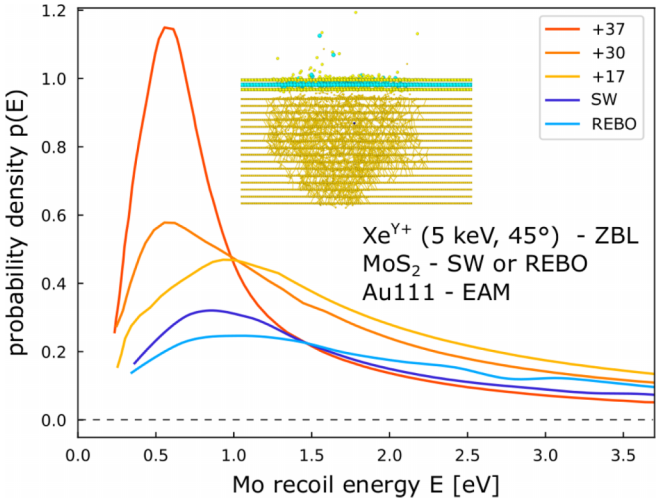

FIG. 5. Probability density of the Mo recoil energy distribution for 5-keV Xe ion impact on 2D MoS_2 supported by Au(111) substrate. The simulation results for two different interaction potentials (SW, REBO) of MoS_2 modeling neutral projectiles are compared to the experimental results for charged Xe (with different charge states). The inset shows a typical atomic configuration just after the ion impact. Cyan balls represent Mo atoms, yellow represents sulfur, and orange represents Au atoms.

IV. CONCLUSIONS

In conclusion, we have succeeded in identifying the mechanisms of material change by HCI irradiation. To do this, we implemented a suitable experimental approach and the distribution of sputtered Mo particles from a MoS_2 layer on different substrates was investigated. We could demonstrate that velocity distributions of particles sputtered from 2D materials can be used to differentiate between various sputtering mechanisms.

From our data we find that the potential energy of a HCI leads to the emission of slow neutral particles from the top layer of the sample. At low kinetic energies, i.e., smaller or comparable to the potential energy, this contribution increases continuously with increasing potential energy. In this regime, there are no significant contributions from either very fast or from ultraslow particles, leading us to rule out Coulomb explosion or nonthermal melting to be the dominant mechanisms. Both take place on ultrashort timescales and would thus lead to particle emission before the collision cascade due to kinetic processes reaches the surface again. However, as our sample material is ultrathin, we would no longer be able to detect the signature of the slower processes, if a significant amount of material had been emitted.

The thermal energies of the emitted atoms point instead towards a mechanism that transfers potential energy from the HCI to the lattice predominantly via electron-phonon coupling. At higher kinetic energies, i.e., a factor of 5 or more in comparison to the potential energy, this fraction can still be identified, but is complemented by a second contribution, which in the case of gold we attribute to the ion induced collisional spike. The two mechanisms are clearly separable and appear to occur independently of each other. These experimental findings are consistent with the results of our atomistic simulations. While our data seems to be in accordance with the corresponding effects simply adding up, synergistic effects are nevertheless still possible, as both mechanisms occur on similar time- and length scales.

Our findings have direct implications for defect engineering of 2D materials. Because the pore creation in 2D materials with HCI proceeds via electron-phonon coupling, the actual pore size, e.g., should depend on the melting temperature of the respective material and should in addition be further tunable by controlling the sample temperature.

ACKNOWLEDGMENTS

The authors acknowledge the German Research Foundation (DFG) by funding through projects SCHL 384/20-1 (Project No. 406129719), C05 (Project No. 278162697) within the SFB1242 "Non-Equilibrium Dynamics of Condensed Matter in the Time Domain," and KR 4866/2-1. The authors also thank the HZDR Computing Center, HLRS, Stuttgart, Germany, and TU Dresden Cluster "Taurus" for generous grants of CPU time.

APPENDIX A: EXPERIMENTAL/EVALUATION DETAILS

Experimental procedures and characterization data for the irradiation and a detailed description of the evaluation of the results are as follows.

To observe the influence of the potential energy, the potential energy E_{pot} is varied from $E_{pot} = 2.996$ keV ($q = 17+$) to $E_{pot} = 38.518$ keV ($q = 40+$). Here, the charge states ($q = 17+$ purple to $40+$ dark red) are chosen to have equidistant potential energy distances of just under $E_{pot} = 9$ keV. Only the measurement point at $E_{pot} = 15.397$ keV ($q = 30+$) is not equidistant to the other measurement points. However, after the first evaluations, it has been decided to include a measurement between $q = 28+$ and $q = 33+$. The chronological

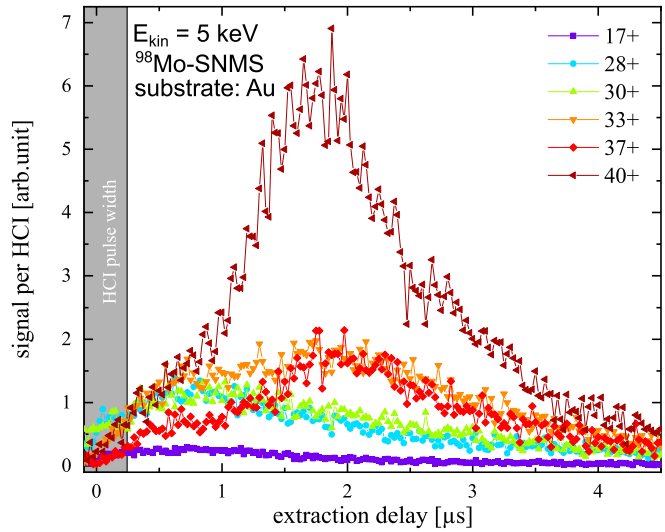

FIG. 6. SNMS data sets of a SL MoS_2/Au sample during bombardment with Xe^{q+} 5-keV ions. The signal is plotted per primary ion over the determined extraction delay. Dark-gray background is the half-width of the broadest primary ion pulse used in this experiment. The lines between the data points are for clarity.

TABLE II. Ion pulse parameters for the $E_{kin} = 5$ keV irradiation.

	E_{pot} (keV)	Ions per pulse	Pulse width (ns)
Xe^{17+}	2.996	4772±447.2	192±10
Xe^{28+}	12.001	1203 ± 120.3	257 ± 25
Xe^{30+}	15.397	998 ± 99.8	390 ± 53
Xe^{33+}	21.165	1040 ± 104	400 ± 51
Xe^{37+}	30.343	674 ± 67.4	410 ± 48
Xe^{40+}	38.518	561 ± 56.1	425 ± 62

TABLE III. Ion pulse parameters for the $E_{kin} = 260$ keV irradiation.

	E_{pot} (keV)	Ions per pulse	Pulse width (ns)
Xe^{26+}	2.996	4772 ± 447.2	192 ± 10
Xe^{28+}	12.001	1203 ± 120.3	257 ± 25
Xe^{30+}	15.397	998 ± 99.8	390 ± 53
Xe^{33+}	21.165	1040 ± 104	400 ± 51
Xe^{37+}	30.343	674 ± 67.4	410 ± 48
Xe^{40+}	38.518	561 ± 56.1	425 ± 62

measurement sequence was deliberately randomized, which means that the different charge states were not measured in ascending or descending order. This ensures that there is no systematic error due to the order of the measurements between the individual charge states. In Fig. 6, the SNMS signal of the ^{98}Mo isotope normalized to the number of respective primary ions is plotted against the extraction delay of the corresponding spectrum. For the extraction delay, the measured hydrogen signals are evaluated and the extraction delay $t = 0$ is determined. The determined half-value widths from the hydrogen signals as well as the primary ion numbers per pulse are given in Table II. In Fig. 6, the half-width around the extraction delay $t = 0$ ns of the broadest hydrogen signal measured in this experiment (FWHM = 425 + 62 ns) is plotted with a dark-gray background, which results from the convolution of the primary ion pulse and the velocity distribution of the atomized hydrogen ions. This is to visually illustrate when the last primary ion triggers a sputtering process in the material. The different potential energies of the primary ions are color-coded from purple (lowest) to dark red (highest). Each measurement point is the integration of the ^{98}Mo isotope SNMS signal at the corresponding extraction delay divided by the number of primary ions. The lines between the measuring points are only for clarity. Based on the fluctuations in the raw data in Fig. 6, it can be assumed that the measurement signal is strongly dependent on the stability of the primary ion current. Especially for highly charged and slow ions with very small ion currents (100 fA), fluctuations in the voltages of, e.g., the EBIS ion source or the lens system for deceleration and focusing, etc., can lead to the primary ion pulse not always hitting the sample system with exactly the same number of particles. This in turn leads to the measurement signal becoming noisy. To counteract this and present the measurement data more clearly, the graphs are smoothed using a Lowess filter with OriginLab 2019b. Comparing the signal intensities in general, it is noticeable that for the Xe^{37+} measurement series, the entire graph is below Xe^{33+} and even below Xe^{28+} and Xe^{30+} at the beginning. As mentioned before, the signal height is significantly influenced by the primary ion number normalization. No current control is performed during the measurement, but before and after the series of measurements for all charge states. Therefore, it cannot be guaranteed that the previously determined ion current is also present during the measurement. In principle, it can be expected that with an increase of the charge state more energy is available for interaction, so that the intensity may at least not become smaller than with lower charge states. For this reason, the measured data for Xe^{37+} are multiplied by a factor of 2.1 so that the signal height is in the range I between Xe^{33+} and Xe^{40+}. A fit for Xe^{17+} is weighted by a factor of 3.0. Care is taken to ensure that at no time is the signal height of the Xe^{17+} measurement greater than in any other measurement. Thus, in addition to smoothing, the measured data are weighted by a factor of 2.1 for Xe^{37+} and by a factor of 3.0 for Xe^{17+}. Figure 1 in the main paper shows these changes.

The normalization to the extraction delay $t = 0$ was done by measuring the signal of the fastest particles (here, hydrogen atoms). A detailed explanation of this, as well as the transformation into a velocity distribution for Fig. 5, can be found in Ref. [19].

APPENDIX B: ION BEAM PARAMETERS

In Tables II and III we collected the beam pulse parameters for all the beams that have been used. The number of primary ions has been measured with a Faraday cup before irradiation. A maximum deviation of 10% has been assumed as the error. The full width at half maximum of the pulse has been determined by a Gaussian fit of the hydrogen signal of every measurement. This method is explained further in Ref. [19].

[1] K. S. Novoselov, A. K. Geim, S. V. Morozov, D. Jiang, Y. Zhang, S. V. Dubonos, I. V. Grigorieva, and A. A. Firsov, Electric field effect in atomically thin carbon films, Science **306**, 666 (2004).

[2] N. Mounet, M. Gibertini, P. Schwaller, D. Campi, A. Merkys, A. Marrazzo, T. Sohier, I. E. Castelli, A. Cepellotti, G. Pizzi, and N. Marzari, Two-dimensional materials from high-throughput computational exfoliation of experimentally known compounds, Nat. Nanotechnol. **13**, 246 (2018).

[3] Y.-H. Lee, X.-Q. Zhang, W. Zhang, M.-T. Chang, C.-T. Lin, K.-D. Chang, Y.-C. Yu, J. T.-W. Wang, C.-S. Chang, L.-J. Li, and T.-W. Lin, Synthesis of large-area MoS_2 atomic layers with chemical vapor deposition, Adv. Mater. **24**, 2320 (2012).

[4] Z. Lin, A. McCreary, N. Briggs, S. Subramanian, K. Zhang, Y. Sun, X. Li, N. J. Borys, H. Yuan, S. K. Fullerton-Shirey, A. Chernikov, H. Zhao, S. McDonnell, A. M. Lindenberg, K. Xiao, B. J. LeRoy, M. Drndić, J. C. M. Hwang, J. Park, M. Chhowalla *et al.*, 2D materials advances: From large scale synthesis and

controlled heterostructures to improved characterization techniques, defects and applications, 2D Mater. **3**, 042001 (2016).

[5] A. K. Geim and I. V. Grigorieva, Van der Waals heterostructures, Nature (London) **499**, 419 (2013).

[6] K. S. Novoselov, A. Mishchenko, A. Carvalho, and A. H. Castro Neto, 2D materials and van der Waals heterostructures, Science **353**, aac9439 (2016).

[7] M. Schleberger and J. Kotakoski, 2D material science: Defect engineering by particle irradiation, Materials **11**, 1885 (2018).

[8] L. Madauß, I. Zegkinoglou, H. Vázquez Muiños, Y.-W. Choi, S. Kunze, M.-Q. Zhao, C. H. Naylor, P. Ernst, E. Pollmann, O. Ochedowski, H. Lebius, A. Benyagoub, B. Ban-d'Etat, A. T. C. Johnson, F. Djurabekova, B. Roldan Cuenya, and M. Schleberger, Highly active single-layer MoS_2 catalysts synthesized by swift heavy ion irradiation, Nanoscale **10**, 22908 (2018).

[9] P. Wang, M. Wang, F. Liu, S. Ding, X. Wang, G. Du, J. Liu, P. Apel, P. Kluth, C. Trautmann, and Y. Wang, Ultrafast ion sieving using nanoporous polymeric membranes, Nat. Commun. **9**, 569 (2018).

[10] T. Foller, L. Madauß, D. Ji, X. Ren, K. K. H. de Silva, T. Musso, M. Yoshimura, H. Lebius, A. Benyagoub, P. V. Kumar, M. Schleberger, and R. Joshi, Mass Transport via In-Plane Nanopores in Graphene Oxide Membranes, Nano Lett. **22**, 4941 (2022).

[11] S. Kretschmer, M. Maslov, S. Ghaderzadeh, M. Ghorbani-Asl, G. Hlawacek, and A. V. Krasheninnikov, Supported two-dimensional materials under ion irradiation: The substrate governs defect production, ACS Appl. Mater. Interfaces **10**, 30827 (2018).

[12] R. Kozubek, M. Tripathi, M. Ghorbani-Asl, S. Kretschmer, L. Madauß, E. Pollmann, M. O'Brien, N. McEvoy, U. Ludacka, T. Susi, G. S. Duesberg, R. A. Wilhelm, A. V. Krasheninnikov, J. Kotakoski, and M. Schleberger, Perforating freestanding molybdenum disulfide monolayers with highly charged ions, J. Phys. Chem. Lett. **10**, 904 (2019).

[13] S. Creutzburg, M. Mergl, R. Hübner, I. Jirka, D. Erb, R. Heller, A. Niggas, P. L. Grande, F. Aumayr, R. A. Wilhelm, M. Kalbac, and S. Facsko, Fluorination of graphene leads to susceptibility for nanopore formation by highly charged ion impact, Phys. Rev. Mater. **5**, 074007 (2021).

[14] E. Gruber, R. A. Wilhelm, R. Pétuya, V. Smejkal, R. Kozubek, A. Hierzenberger, B. C. Bayer, I. Aldazabal, A. K. Kazansky, F. Libisch, A. V. Krasheninnikov, M. Schleberger, S. Facsko, A. G. Borisov, A. Arnau, and F. Aumayr, Ultrafast electronic response of graphene to a strong and localized electric field, Nat. Commun. **7**, 13948 (2016).

[15] J. Schwestka, H. Inani, M. Tripathi, A. Niggas, N. McEvoy, F. Libisch, F. Aumayr, J. Kotakoski, and R. A. Wilhelm, Atomic-scale carving of nanopores into a van der Waals heterostructure with slow highly charged ions, ACS Nano **14**, 10536 (2020).

[16] F. Aumayr, S. Facsko, A. S. El-Said, C. Trautmann, and M. Schleberger, Single ion induced surface nanostructures: A comparison between slow highly charged and swift heavy ions, J. Phys.: Condens. Matter **23**, 393001 (2011).

[17] E. Pollmann, L. Madauß, V. Zeuner, and M. Schleberger, Strain in single-layer MoS_2 flakes grown by chemical vapor deposition, in *Encyclopedia of Interfacial Chemistry* (Elsevier, New York, 2018), pp. 338–343.

[18] E. Pollmann, L. Madauß, S. Schumacher, U. Kumar, F. Heuvel, C. vom Ende, S. Yilmaz, S. Güngörmüs, and M. Schleberger, Apparent differences between single layer molybdenum disulphide fabricated via chemical vapour deposition and exfoliation, Nanotechnology **31**, 505604 (2020).

[19] L. Skopinski, P. Ernst, M. Herder, R. Kozubek, L. Madauß, S. Sleziona, A. Maas, N. Königstein, H. Lebius, A. Wucher, and M. Schleberger, Time-of-flight mass spectrometry of particle emission during irradiation with slow, highly charged ions, Rev. Sci. Instrum. **92**, 023909 (2021).

[20] S. Plimpton, Fast parallel algorithms for short-range molecular dynamics, J. Comput. Phys. **117**, 1 (1995).

[21] T. Liang, S. R. Phillpot, and S. B. Sinnott, Erratum: Parametrization of a reactive many-body potential for Mo–S systems [Phys. Rev. B 79, 245110 (2009)], Phys. Rev. B **85**, 199903(E) (2012).

[22] J.-W. Jiang, H. S. Park, and T. Rabczuk, Molecular dynamics simulations of single-layer molybdenum disulphide (MoS_2): Stillinger-Weber parametrization, mechanical properties, and thermal conductivity, J. Appl. Phys. **114**, 064307 (2013).

[23] G. J. Ackland, G. Tichy, V. Vitek, and M. W. Finnis, Simple *N*-body potentials for the noble metals and nickel, Philos. Mag. A **56**, 735 (1987).

[24] J. F. Ziegler and J. P. Biersack, The stopping and range of ions in matter, in *Treatise on Heavy-Ion Science*, edited by D. A. Bromley (Springer US, Boston, MA, 1985), pp. 93–129.

[25] A. Arnau, F. Aumayr, P. M. Echenique, M. Grether, W. Heiland, J. Limburg, R. Morgenstern, P. Roncin, S. Schippers, R. Schuch, N. Stolterfoht, P. Varga, T. Zouros, and H. P. Winter, Interaction of slow multicharged ions with solid surfaces, Surf. Sci. Rep. **27**, 113 (1997).

[26] F. Aumayr and H. Winter, Potential sputtering, Philos. Trans. Ser. A **362**, 77 (2004).

[27] P. Sigmund, Sputtering by ion bombardment theoretical concepts, in *Sputtering by Particle Bombardment I, Topics in Applied Physics*, edited by R. Behrisch (Springer, Berlin, Heidelberg, 1981), Vol. 47, pp. 9–71.

[28] I. S. Bitensky and E. S. Parilis, Shock wave mechanism for cluster emission and organic molecule desorption under heavy ion bombardment, Nucl. Instrum. Methods Phys. Res. Sect. B **21**, 26 (1987).

[29] H.-P. Cheng and J. D. Gillaspy, Nanoscale modification of silicon surfaces via Coulomb explosion, Phys. Rev. B **55**, 2628 (1997).

[30] T. Schenkel, A. V. Hamza, A. V. Barnes, D. H. Schneider, J. C. Banks, and B. L. Doyle, Ablation of GaAs by Intense, Ultrafast Electronic Excitation from Highly Charged Ions, Phys. Rev. Lett. **81**, 2590 (1998).

[31] R. Stoian, D. Ashkenasi, A. Rosenfeld, and E. E. B. Campbell, Coulomb explosion in ultrashort pulsed laser ablation of Al_2O_3, Phys. Rev. B **62**, 13167 (2000).

[32] M. Toulemonde, C. Dufour, and E. Paumier, Transient thermal process after a high-energy heavy-ion irradiation of amorphous metals and semiconductors, Phys. Rev. B **46**, 14362 (1992).

[33] O. Osmani, N. Medvedev, M. Schleberger, and B. Rethfeld, Energy dissipation in dielectrics after swift heavy-ion impact: A hybrid model, Phys. Rev. B **84**, 214105 (2011).

[34] L. Madauß, O. Ochedowski, H. Lebius, B. Ban-d'Etat, C. H. Naylor, A. T. C. Johnson, J. Kotakoski, and M.

Schleberger, Defect engineering of single- and few-layer MoS_2 by swift heavy ion irradiation, 2D Mater. **4**, 015034 (2017).

[35] M. P. Seah, Analysis of cluster ion sputtering yields: Correlation with the thermal spike model and implications for static secondary ion mass spectrometry, Surf. Interface Anal. **39**, 634 (2007).

[36] R. Kozubek, P. Ernst, C. Herbig, T. Michely, and M. Schleberger, Fabrication of defective single layers of hexagonal boron nitride on various supports for potential applications in catalysis and DNA sequencing, ACS Appl. Nano Mater. **1**, 3765 (2018).

[37] A. V. Krasheninnikov, Are two-dimensional materials radiation tolerant?, Nanoscale Horizons **5**, 1447 (2020).

[38] J. F. Ziegler, M. D. Ziegler, and J. P. Biersack, SRIM – The stopping and range of ions in matter (2010), Nucl. Instrum. Methods Phys. Res. Sect. B **268**, 1818 (2010).

[39] O. Ochedowski, B. K. Bussmann, and M. Schleberger, Graphene on mica-Intercalated water trapped for life, Sci. Rep. **4**, 6003 (2014).